energy&fuels

pubs.acs.org/EF

Article

Fine-Tuning the Activity Volcano of Single-Atom Iron Catalysts in NH_3−SCR Regulated by Local Coordination Environment

Zhengyang Gao, Chu Wang, Mingzhe Li, Ziwei Miao, Yuxuan Liu, Kewen Guo, Yongqian Zhang, and Weijie Yang*

Cite This: *Energy Fuels* 2025, 39, 4471−4480

Read Online

ACCESS | Metrics & More | Article Recommendations | Supporting Information

ABSTRACT: Although advanced single-atom catalysts (SACs) have demonstrated remarkable performance in various catalytic fields, their application in selective catalytic reduction with ammonia (NH_3−SCR) remains challenging due to the lack of fundamental theoretical guidance. To address this, we propose a strategy for regulating the local coordination environment by modulating the coordination of nonmetal elements around the metal center, aiming to fine-tune the catalytic activity of SACs for NH_3−SCR. In this study, seven theoretical models of single-atom iron catalysts anchored on double-vacancy graphene substrates doped with three nitrogen atoms and one nonmetal atom (Fe−N_3X, X = B, C, N, O, S, P, Cl) are constructed. The reaction pathways of these Fe−N_3X catalysts in NH_3−SCR have been systematically investigated. The activity volcano map of NH_3−SCR based on the NO_2 adsorption energy is established, and the catalytic activities of 30 different SACs are evaluated. Regulating the local coordination environment of the single-atom iron catalyst can fine-tune the active volcano map of the catalyst in a small range (activity, −0.7 to −1.6), while changing the active center can roughly regulate the volcano map in a wide range (activity, −0.8 to −3.5). Based on this fine-tuning strategy, we successfully improve the catalytic activities of single-atom Zn and Mn catalysts by modulating the types of coordinated nonmetal atoms. Furthermore, a linear relationship between charge transfer and NO_2 adsorption energy is established, providing insights into the origin of the activity fine-tuning strategy at the electronic structure level. This work provides a novel approach to catalyst activity regulation and offers valuable guidance for designing advanced NH_3−SCR catalysts.

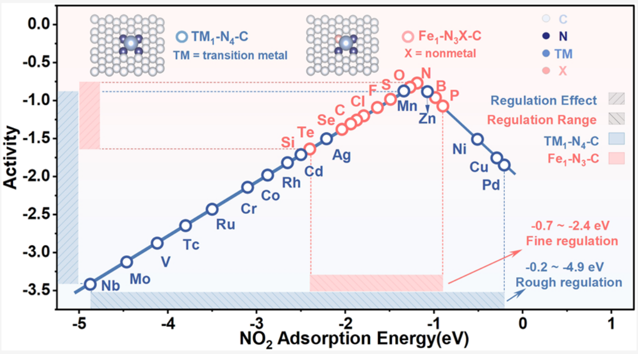

1. INTRODUCTION

Coal-fired power plants are one of the main sources of atmospheric pollutants,[1,2] and nitrogen oxides (NO_x) in the discharged flue gas can lead to natural disasters such as acid rain and photochemical smog.[3−5] With the increasingly serious problems of air pollution, the treatment and control of NO_x have become an important task at the current stage.[6−8] The most widely used postcombustion removal technologies can be divided into selective noncatalytic reduction (SNCR) and selective catalytic reduction (SCR); the SCR technology using ammonia as a reducing agent (NH_3−SCR) is the most effective and widely used denitration technology at present.[9,10] The catalyst is the core of the SCR technology, which greatly affects the denitration efficiency and cost.[11] NH_3−SCR catalysts can be divided into metal oxide-based SCR catalysts, carbon-based SCR catalysts, and mineral-based SCR catalysts; among them, vanadium-based catalysts are the commercially widely used SCR catalysts,[11,12] and their NO_x conversion rate can exceed 90%[13] under the optimal operating temperature (300−400 °C). However, in recent years, the grid connection of renewable energy has made the low-load operation of the power grid become a new trend, and the load reduction of the unit will cause the inlet temperature of the SCR device far less than its optimal operating temperature, resulting in a large reduction of its catalytic activity.[14,15] Wang et al.[16] study the poisoning mechanism of the V_2O_5−WO_3/TiO_2 catalyst and find that the catalyst has better sulfur resistance at high temperatures; when it works at low temperatures, not only the denitration efficiency will be greatly reduced but also the sulfur and water resistance will be decreased, resulting in catalyst poisoning or even deactivation. In addition, discarded vanadium-based catalysts are highly toxic to the environment,[17] which is difficult to treat and recycle. Therefore, it is necessary to find alternative new NH_3−SCR catalysts, which

Received: December 10, 2024
Revised: February 8, 2025
Accepted: February 17, 2025
Published: February 21, 2025

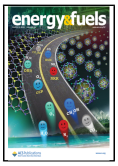

https://doi.org/10.1021/acs.energyfuels.4c06055

are environmentally friendly and have high activity and excellent sulfur and water resistance at low temperatures.

Recently, the catalysts in which the metal atoms are dispersed in the form of single atoms on support are called single-atom catalysts (SACs);[18,19] especially, the SACs synthesized by embedding transition-metal atoms in graphene-based substrates (TM/GS) have attracted much attention due to their environmental protection, high catalytic activity, and high selectivity;[20,21] it provides a new way to solve the above problems. Li et al.[22] investigate the adsorption properties of graphene-based single-atom nickel (Ni) adsorbent on acid gases in flue gas and conclude that Ni-SVN$_3$/GN is a suitable adsorbent for acid gas removal. Yang et al.[3] develop the Fe$_1$−N$_4$−C catalyst (a single-atom iron catalyst doped with four N atoms with a double-vacancy graphene substrate) and find that Fe$_1$−N$_4$−C has a high catalytic activity of NO and Hg^0 oxidations at 200 °C, far exceeding that of traditional SCR catalysts, and also has a strong sulfur resistance. Chen et al.[23] use 10 TM$_1$-N$_4$−C (TM = transition metal) as catalysts to oxidize Hg^0 and construct an active volcano map using the adsorption energy (E_{ads}) of atom O as a descriptor. Similarly, they also explore the reaction paths of NO oxidation using OH radical on 8 TM$_1$-N$_4$−C and establish the volcano map with OH adsorption energy as a description factor.[24] The results show that Fe$_1$−N$_4$−C has the highest catalytic activity in 3d, 4d, and 5d SACs for the catalytic oxidation of Hg^0 and NO.

A large number of studies have shown that Fe$_1$−N$_4$−C has high activity in the field of catalytic oxidation of NO, so it is reasonable to guess that it may also have high activity in the NH$_3$−SCR reaction. Yang et al.[25] explore the possibility of Fe$_1$−N$_4$−C as NH$_3$−SCR by constructing seven possible NH$_3$−SCR reaction paths on Fe$_1$−N$_4$−C. The RDS energy barrier of the major reaction path is 0.99 eV, indicating that Fe$_1$−N$_4$−C is a potential NH$_3$−SCR catalyst. However, the current understanding of the NH$_3$−SCR reaction mechanism on a single-atom iron catalyst is still shallow, only focusing on the possible reaction paths in Fe$_1$−N$_4$−C. There is a gap in the understanding of the catalyst activity source in the NH$_3$−SCR reaction, which cannot guide the optimization design of new SCR catalysts. Therefore, it is necessary to further explore the relationship between the properties of the single-atom iron catalyst and catalytic activity in the NH$_3$−SCR reaction.

Previous studies on the relationship between catalyst properties and catalyst activity can be divided into two categories: one is to adjust the catalyst performance by changing the metal active center[24] and visually display the relationship between the catalyst structure and catalytic activity by mapping the catalyst activity into an activity volcano map. The horizontal axis of the volcano map is generally the adsorption energy of the substrate to a certain reaction substance; its range can reflect the regulation range of the catalyst activity. The vertical axis is generally the reactivity, and its range can reflect the regulation effect of the method. As the metal active center has a great influence on the catalyst properties, the catalysts with different metal centers in the volcano map have a great difference in activity, which leads to rough regulation, and it is not possible to fine-regulate the properties of the catalyst to make it fall into the activity interval required for the reaction. The other is to adjust the performance of the catalyst by adjusting the local coordination environment, such as doping nonmetallic elements on the catalyst substrate.[26,27] Zhou et al.[27] propose a method to reduce the reaction energy barrier by doping different p-block elements to adjust the coordination environment of a single-atom cobalt (Co) catalyst. Compared with the previous regulation method of changing the metal active center ($E_{\text{ads(O)}}$, −4 to 0.5 eV),[24] this method can achieve a fine regulation of the catalyst adsorption properties ($E_{\text{ads(O)}}$, −0.24 to −1.98 eV).

Herein, Fe$_1$−N$_4$−C is selected as the research object, and we construct seven theoretical models through doping nonmetal atoms (Fe−N$_3$X, X═C, N, O, S, B, P, and Cl). The adsorption characteristics of seven catalysts on the main components (H$_2$O, NH$_3$, NO$_2$, NO, SO$_2$, and O$_2$) in flue gas are first studied. Second, the NH$_3$−SCR reaction paths of a single-atom iron catalyst regulated are explored by adjusting the adsorption order of the reaction gas. Finally, the reaction mechanisms are further studied by microkinetic analysis; we construct an active volcano map and predict the activities of 30 SACs. The catalysts with lower energy barriers are screened out, which provides a theoretical basis for the subsequent theoretical calculation and experimental preparation.

2. CALCULATIONS AND METHODS

Compared with traditional experimental research, density functional theory (DFT) calculation is often used to predict and search material properties with its low computing cost, accuracy, and efficient characteristics.[28−30] In this article, the Vienna Ab initio Simulation Package (VASP) software and the projector-enhanced wave (PAW) method were used for all simulation calculations. Generalized gradient approximation (GGA) and Perdew−Burke−Ernzerhof (PBE) functionals were used to deal with exchange-related interactions.[31−34] According to the electronic structure of the iron atom, considering the spin polarization effect (ISPIN = 2),[35] the electron energy level was occupied by Gaussian smearing with a width of $\sigma = 0.05$ eV.[36] In order to reduce the calculation time as much as possible under the premise of ensuring the calculation accuracy, the cutoff energy and k-points were tested, respectively (Figure S1). A 4 × 4 × 1[37] supercell of graphene was constructed as catalyst support, and the vacuum layer was set to 15 Å[38] to avoid the interaction between the mirror images. The geometry was optimized using a 2 × 2 × 1 Γ-center k-point with an energy cutoff of 450 eV and a force convergence criterion of 0.02 eV/Å for each atom.[39] Then, a 4 × 4 × 1 Γ-center k-point was used for electronic self-consistent calculations, and the convergence standard was 1×10^{-5} eV. The climbing image nudged elastic band (CINEB) method combined with improved dimer method (IDM) was used to find the transition-state structure of the reaction.[40] First, the approximate position of the reaction path and transition-state structure was roughly obtained by the CINEB method; then, the reaction frequency was calculated to ensure that there was only one virtual frequency and the vibration direction of the frequency was consistent with the reaction direction, and the finite displacement of the vibration frequency was ±0.02 Å.[41] Finally, the initial guess structure was accurately calculated by the IDM method, and the force convergence criterion was 0.05 eV/Å.[42,43] To investigate the relationship between the adsorption energy of the gas on the catalyst and the charge distribution of the system, we also performed a charge density difference (CDD) analysis. CDD is one of the most popular methods of analyzing the electronic structure. The distribution of electrons in space is an electron cloud, and the charge density difference is the difference between the atomic charge density at the corresponding points before and after an interaction of atoms.[44] The formula is calculated as follows[45]

$$\Delta\rho = \rho_{\text{absorb}} - \rho_{\text{sur}} - \rho_{\text{gas}}$$

where ρ_{absorb}, ρ_{sur}, and ρ_{gas} are the charge densities of the adsorption system, catalyst surface, and gas, respectively.

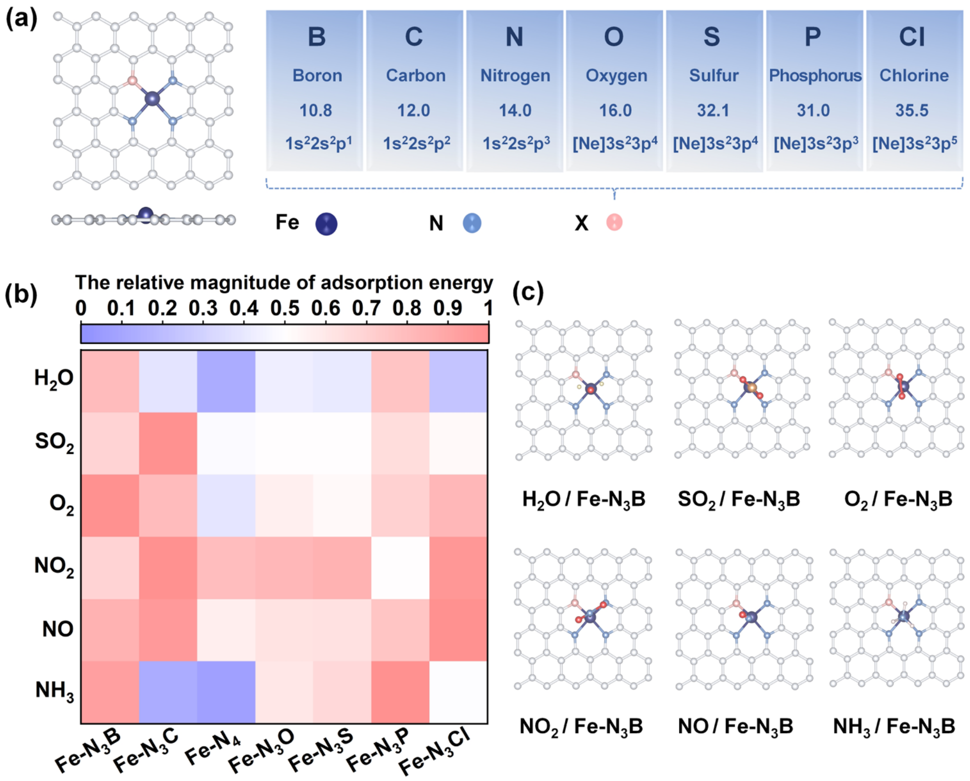

Figure 1. (a) The configuration of the catalyst doped with nonmetal atoms and seven kinds of nonmetal coordination atoms. (b) The relative adsorption energy of each substrate to each gas. Here, the adsorption energy of each gas is normalized separately, and the reference standard is the maximum absolute value of the adsorption energy of the catalyst for each gas. (c) Stable adsorption configuration of H_2O, SO_2, NO_2, NO, O_2, and NH_3 on Fe−N_3B.

Table 1. Adsorption Height (h, Å), Bond Length between Fe Atom and Doping Atom (d, Å), Number of Electrons Transferred from the Fe Atom to Carrier (Δq, e), Binding Energy (E_b, eV), and Magnetic Moment (M, μ_B)[a]

catalyst	h(Å)	d(Å)	Δq(e)	E_b(eV)	M(μ_B)
Fe−N_3B	0.05	1.88	0.85	5.45	2.58
Fe−N_3C	0.05	1.87(1.89[4])	1.00	6.33(6.47[39])	2.36
Fe−N_4	0.05(0.05[46])	1.89(1.89[46])	1.03(1.08[46])	7.14(7.13[27])	2.00(2.00[46])
Fe−N_3O	0.05	1.95(1.93[4])	0.96	5.63	1.38
Fe−N_3S	0.07	2.11	0.90	5.46	1.47
Fe−N_3P	0.05	2.17(2.17[4])	0.92	6.05(6.47[39])	1.99
Fe−N_3Cl	0.07	2.05	0.86	4.20	1.03

[a] The contents in parentheses are the results of previous studies of the corresponding items.

3. RESULTS AND DISCUSSION

3.1. Catalyst Model. Fe_1−N_4−C is selected as the model catalyst, and we obtain 7 catalyst configurations (Figure 1a) (Fe−N_3X, X = coordination atom) by using different coordination atoms (B, C, N, O, S, P, Cl) to replace one of the four N atoms in the substrate. The corresponding bond length,[43] transfer electron, binding energy, and magnetic moment are shown in Table 1. All seven catalysts have high binding energy and good stability. In addition, the calculated results of seven single-atom iron catalysts are in good agreement with the previous results,[4,39,43] which verifies the rationality and validity of this work.

3.2. Adsorption Behavior. In order to explore how the local coordination environment regulates the properties of catalysts, this section first discusses its influence on the adsorption properties of each catalyst. Since there are many intermediate states and products involved in the NH_3−SCR reaction, we select six main gases here and calculate their adsorption energies on the catalysts (see S1 for the specific calculation formula of adsorption energy). In order to facilitate the comparison of the differences in the adsorption strength of different catalysts for different gases, the adsorption energy is normalized and the heat map is drawn, as shown in Figure 1b (see Table S2 for the specific values of adsorption energy of each catalyst for the adsorption of different gases, Figure S2 for the stable configuration of adsorbing NH_3, SO_2, and H_2O, and Figure S3 for the stable configuration of adsorbing O_2, NO_2, and NO).

On the different catalysts, the adsorption energy of the same gas on each substrate is different, and the local coordination environment regulation has a great influence on the adsorption energy of each gas on the catalyst. Therefore, we can adjust the catalyst properties by regulating the local coordination environment of the catalysts. In addition, in the gases discussed above, NH_3, NO_2, NO, and O_2 participate in the reaction process and promote the reaction, while H_2O and SO_2

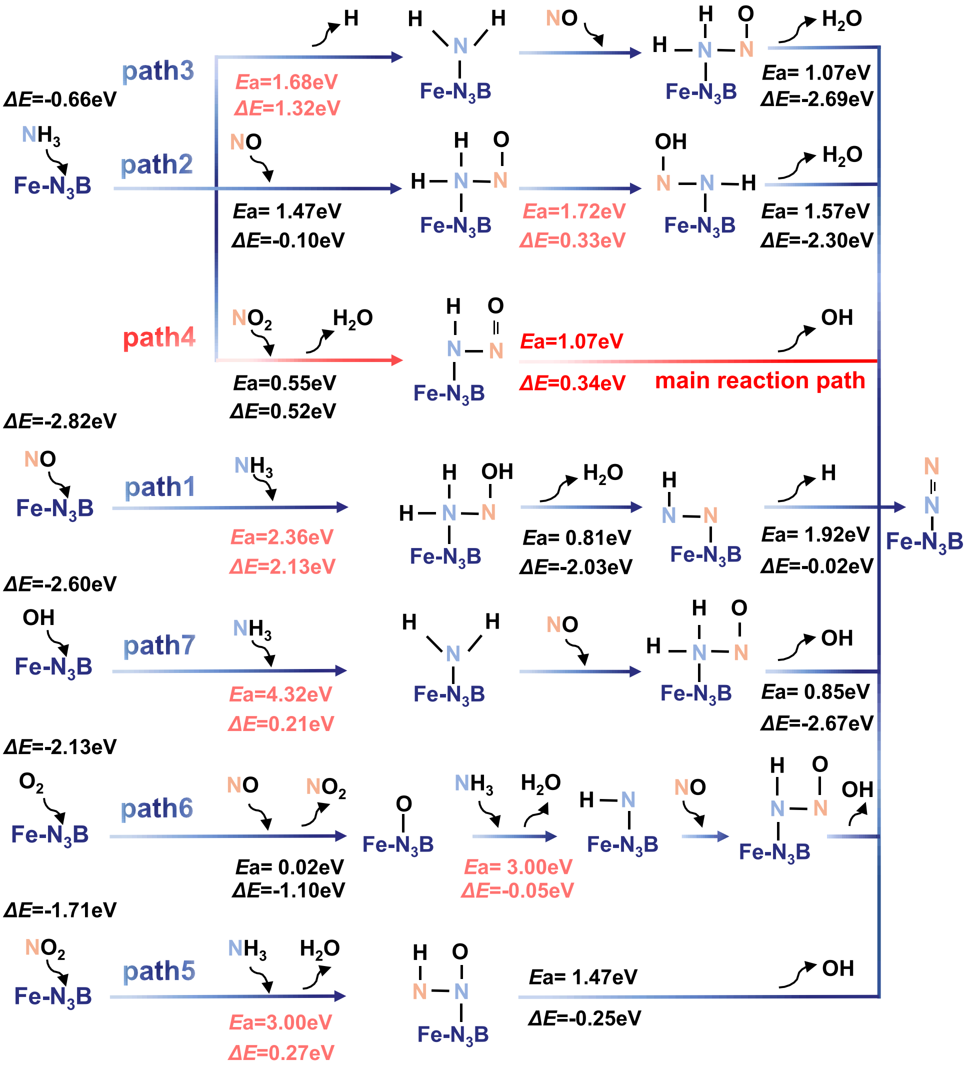

Figure 2. All reaction paths in the NH_3−SCR reaction on Fe−N_3B. The diagram of the N atom in the NH_3 molecule is represented in blue, and the diagram of the N atom in NO and NO_2 is represented in orange. In the seven reaction paths, the ΔE_{RDS} of each reaction path is marked in red in the figure and the unit is eV.

preempt the active site and hinder the reaction. The Fe−N_3B catalyst has strong adsorption of NO_2, NO, O_2, and NH_3 and weak adsorption of H_2O and SO_2 (the stable adsorption configuration of NO_2, NO, O_2, H_2O, and NH_3 on Fe−N_3B is shown in Figure 1c), which is beneficial to the NH_3−SCR reaction, so the Fe−N_3B catalyst is selected to further study the NH_3−SCR reaction mechanism on the catalyst surface, and the detailed work is shown in the next section.

3.3. Reaction Path Analysis of NH_3−SCR on Fe−N_3X (X═B, C, N, O, S, P, Cl). Previous studies show that NH_3−SCR reaction paths on catalysts are complicated, but the energy barrier of each path is very different, and many paths are difficult to occur.[47] In order to save the calculation cost, this section discusses all reaction paths based on Fe−N_3B and screens out the main reaction path to lay the groundwork for the subsequent construction of the volcano map. Referring to previous studies of NH_3−SCR reactions on Fe_1−N_4−C, we construct seven possible paths. The construction of the whole reaction path is based on the adjustment of the adsorption order on the catalyst, including NH_3 adsorption, NO adsorption, NO_2 adsorption, and O_2 adsorption. Since the ·OH generated by the reaction can also participate in the NH_3−SCR reaction as an active radical, the reaction paths of the adsorption of ·OH and the removal of residual H atom are also considered.[17,47]

Figure 2 shows the complete reaction system of NH_3−SCR on the surface of the Fe−N_3B catalyst and RDS energy barrier (ΔE_{RDS}) of each path. The ΔE_{RDS} of path 4 is 1.07 eV, much lower than 2.36 eV for path 1, 1.72 eV for path 2, 1.68 eV for path 3, 3.00 eV for path 5, 3.00 eV for path 6, and 4.32 eV for path 7 (the optimized structures of paths 1−8 and calculated free-energy diagrams of each path on Fe−N_3B are shown in Figures S4−S6). The paths with higher RDS energy barriers are less likely to occur. So, path 4 is most likely to occur and can be considered the main reaction path of NH_3−SCR catalyzed by the Fe−N_3B catalyst, which is conducive to N_2 formation.

In order to explore the mechanism of the NH_3−SCR reaction on the surface of a single-atom iron catalyst regulated by a local coordination environment, the main reaction path (path 4) is constructed on the other six catalyst substrates (Fe−N_3X, X = C, N, O, S, P, Cl). As shown in Figure 3a, the first step of the reaction is the reaction of NH_3 and NO_2 molecules on each substrate to generate the intermediate

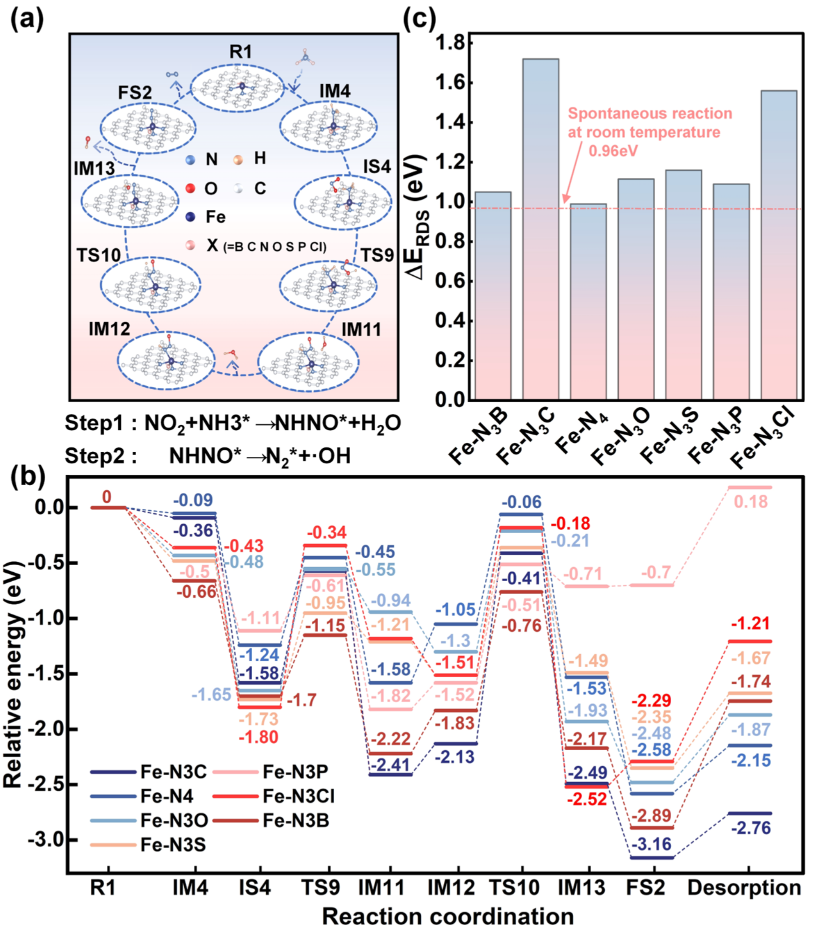

Figure 3. (a) Reaction scheme of path 4 on the Fe−N$_3$X catalyst. (b) Relative energy step diagram of path 4 on seven catalysts for NH$_3$−SCR. (c) The ΔE_{RDS} of path 4 on different catalysts.

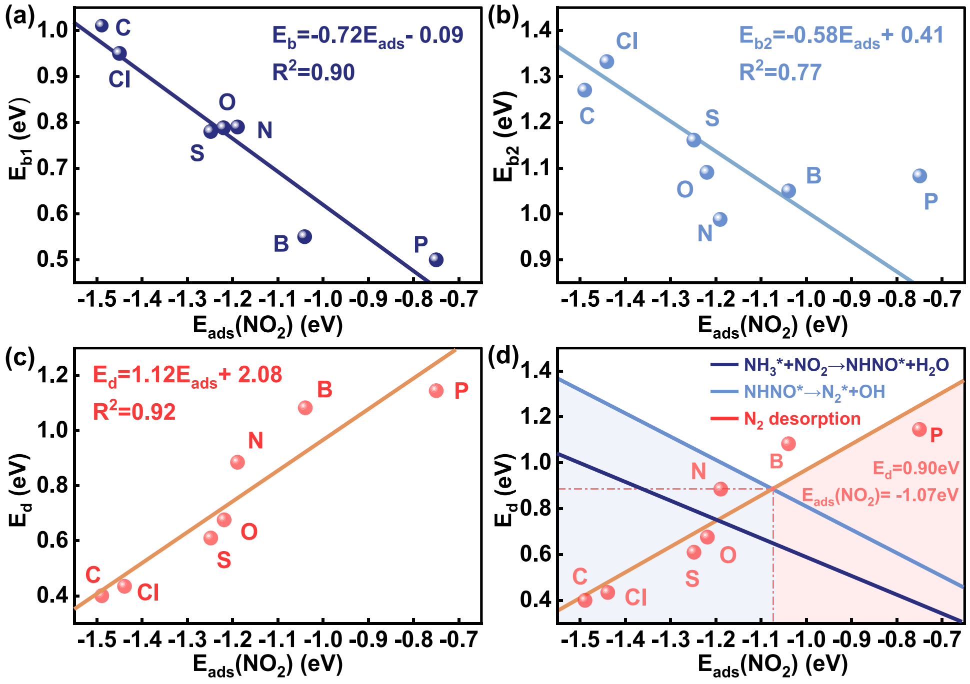

Figure 4. (a) Correlation analysis between E$_{b1}$ and $E_{ads\ (NO2)}$. (b) Correlation analysis between E$_{b2}$ and $E_{ads\ (NO2)}$. (c) Correlation analysis between E$_d$ and $E_{ads\ (NO2)}$. (d) Correlation analysis between the energy barrier and $E_{ads\ (NO2)}$. The dark blue, light blue, and orange lines represent the first and second reaction energy barriers of NH$_3$ reduction and the desorption energy barriers of N$_2$ molecules, respectively.

https://doi.org/10.1021/acs.energyfuels.4c06055

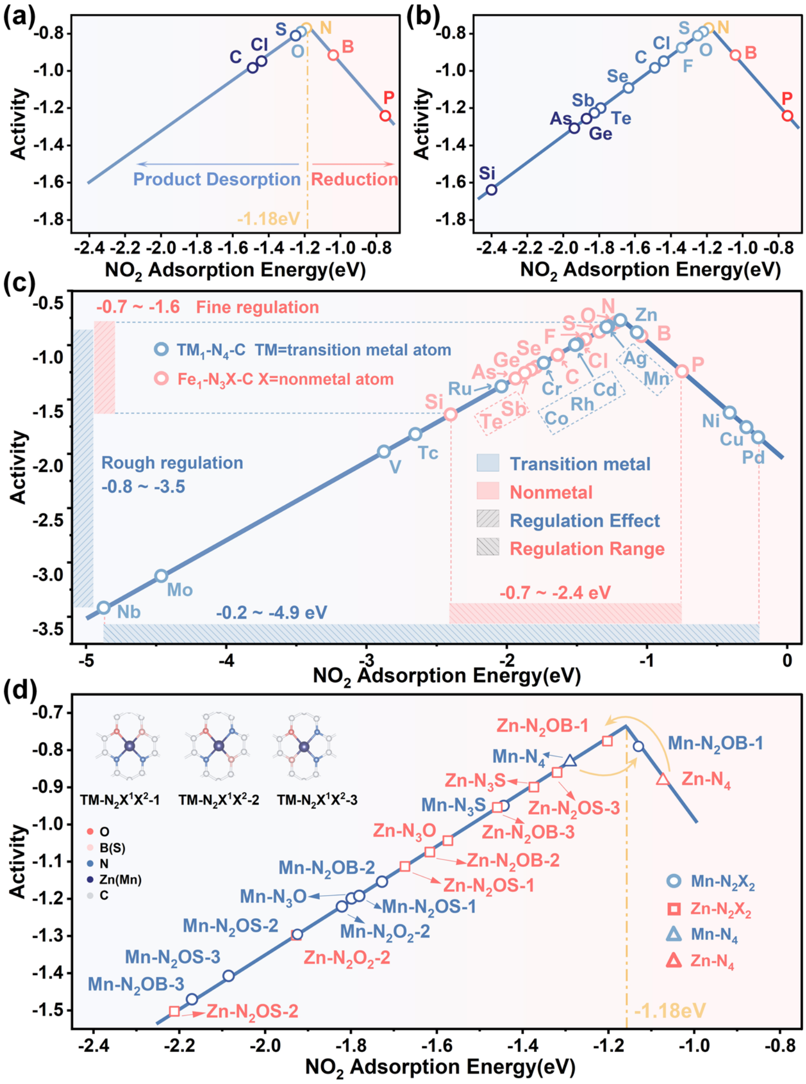

Figure 5. (a) Volcano plots as a function of NO_2 adsorption energy with 7 SACs. (b) Volcano plots as a function of NO_2 adsorption energy with 14 nonmetal SACs (Fe−N_3X, X = nonmetal or metal-like atom). (c) Comparison of volcano maps for transition metal and nonmetal SACs. (d) Fine-tuning the activity of Zn−N_4 and Mn−N_4 by doping with nonmetal atoms. Gray, light blue, blue, red, and pink atoms represent C, N, Fe, and O and doping nonmetal atom, respectively.

NHNO* and H_2O molecules; the second step of the reaction is the decomposition process of the intermediate NHNO*, and the final step is the desorption of the generated nitrogen.

To analyze the energy change of path 4 on each substrate more intuitively, the energy step diagram of seven catalysts is constructed. In Figure 3b, the substrate is set to zero-energy state, and the energy of each intermediate state is determined relative to the ground state under the condition that each intermediate state satisfies proton conservation (the reaction path diagrams of path 4 over Fe−N_3X are shown in Figures S7 and S8). The reaction on these substrates depends on the step with the highest barrier, which is the RDS.

By comparing the reaction energy barrier and the desorption energy barrier, these catalysts can be divided into two categories. One is that the reaction energy barrier is the highest; the rate-determining step is the first step or the second step of the reaction process, such as Fe−N_3B, Fe−N_3C, Fe−N_4, Fe−N_3O, Fe−N_3S, and Fe−N_3Cl. The other class is that the desorption energy barrier is the highest; the rate-determining step is the product desorption process, such as Fe−N_3P. As shown in Figure 3c, the RDS energy barriers of Fe−N_4 and Fe−N_3B are closest to 0.96 eV, indicating that both catalysts have good catalytic activity at near room temperature. Compared with previous studies, they also exhibit superior performance (see Table S1 for the RDS energy barriers of previous studies). According to the above analysis, a catalyst with good performance should have an appropriate reaction energy barrier and desorption energy barrier, which provides an idea for the subsequent construction of the activity volcano map.

3.4. Correlation Analysis.

Based on Brønsted−Evans−Polanyi (BEP) rule,[42,43] reaction kinetics are usually related to thermodynamics on heterogeneous catalytic surface, and the adsorption strength of gas molecules on the catalyst surface directly affects the catalytic activity and selectivity of the catalytic reaction.[46,48−50] Figure 4 discusses the correlation between the adsorption energy of NO_2 ($E_{ads(NO2)}$) and the energy barrier of the first and second steps (E_{b1},E_{b2}) in the NH_3 reduction reaction and the correlation between the $E_{ads(NO2)}$ and the desorption energy barrier of N_2(E_d).

As shown in Figure 4a−c, the $E_{\mathrm{ads(NO2)}}$ is linearly correlated to the kinetic energy barriers of all of the reactions analyzed in this study. The E_{b1} and E_{b2} of the NH_3 reduction decrease with the increase of $E_{\mathrm{ads(NO2)}}$, indicating that within a certain range, the promotion effect of the substrate on the NH_3−SCR reaction becomes stronger with the increase of $E_{\mathrm{ads(NO2)}}$. At the same time, the E_d of NH_3 reductions increases with the increase of $E_{\mathrm{ads\ (NO2)}}$, indicating that the ΔE_{RDS} of the NH_3 reduction is affected by three reaction stages simultaneously and depends on the maximum energy barrier of the three stages. Figure 4d compares the relationship between $E_{\mathrm{ads(NO2)}}$ and E_{b1}, E_{b2}, and E_d of a single reaction. The ΔE_{RDS} of the NH_3 reduction depends on the maximum energy barriers in the three reaction stages. The adsorption energy of NO_2 at −1.07 eV corresponds to the maximum energy barrier of the three stages. When $E_{\mathrm{ads(NO2)}}$ is greater than −1.07 eV, RDS represents the desorption process of N_2 from the catalyst surface, indicating that too weak adsorption leads to difficulties in reactant activation, reaction process, and product desorption. When $E_{\mathrm{ads(NO2)}}$ is less than −1.07 eV, the RDS represents the progress of the first reaction, indicating that the adsorption capacity is too strong and the subsequent reaction is difficult to occur. Among the seven SACs, Fe−N_3B has a lower energy barrier during the NH_3 reduction. When $E_{\mathrm{ads(NO2)}}$ reaches −1.07 eV, the energy barrier of SACs reaches the lowest, and the optimal energy barrier is 0.90 eV. In conclusion, the adsorption energy of NO_2 can be a highly accurate descriptor to help predict other complex kinetic information in the calculation of the NH_3 reduction.

3.5. Microkinetic Analysis.

Through the correlation analysis above, the reaction of NO_2 and NH_3* on SACs also follows the classical Sabatier principle,[51] that is, an ideal heterogeneous catalyst should not be too strongly or weakly bound to the adsorbents. Based on the high correlation between the adsorption energy of NO_2 and the energy barrier, the microkinetic activity volcano plot is established with $E_{\mathrm{ads\ (NO2)}}$ as the basic reaction descriptor (see S2 for details on the microkinetic modeling method). On this basis, we calculate the NO_2 adsorption energy of catalysts doped with several other atoms (Si, As, Ge, Sb, Te, Se) and obtain the theoretical predicted value of their reactivity (Figure 5b).

These doping atoms have similar properties to the doping atoms discussed above, and all belong to the two categories of elements: metal-like and nonmetal atoms. Fe−N_3B and Fe−N_4 show a higher activity among the 14 kinds of catalysts. In addition, we calculate the NO_2 adsorption energy of 16 kinds of catalysts (TM_1-N_4−C, TM = V- Cd) with 3d and 4d transition metals as the active center, respectively, and obtain the corresponding volcano map (Figure 5c) (see Table S2 for the specific values of adsorption energy of Fe−N_3X and Table S3 for the specific values of adsorption energy of TM_1-N_4−C). Figure 5c shows that the method of changing the active center can roughly regulate the volcano map in a wide range ($E_{\mathrm{ads(NO2)}}$, −0.2 to −4.9 eV; activity, − 0.8 to − 3.5), while the method of regulating the local coordination environment of the single-atom iron catalyst can fine-tune the active volcano map of the catalyst in a small range ($E_{\mathrm{ads(NO2)}}$, −0.7 to −2.4 eV; activity, − 0.7 to − 1.6).

To further verify the validity of this regulation method, we fine-tune the catalytic activity of Mn−N_4 and Zn−N_4 near the peak of the volcano map by doping nonmetal atoms. As shown in Figure 5d, we dope a single nonmetal atom (O, S) on the substrate; the results show a decrease in the catalyst activity after doping, so we try to dope two different nonmetal atoms on the substrate. According to the symmetry of TM_1-N_4−C, there are three different types of doping types. By doping two nonmetal atoms (O and B), we have further improved the activity of the single-atom Zn/Mn catalyst, which is closer to the peak of the activity volcano map. Above all, this regulation method not only provides a new idea for the regulation of the catalyst activity but also facilitates the development of NH_3−SCR single-atom catalysts with better performance.

3.6. Electronic Characteristics.

In order to analyze the reasons for the adsorption energies of NO_2 between different SACs from the microelectronic level, the charge density difference and Bader charge analysis are carried out between different SACs and NO_2.

As shown in Figure 6, there exists a negative linear relationship between the NO_2 adsorption energy and charge transfer of NO_2. On the surface of Fe−N_3Si, both Fe and Si provide electrons to NO_2, which strengthens the NO_2 adsorption of the substrate but is also not conducive to product desorption. From Fe−N_3Si to Fe−N_3P, the $E_{\mathrm{ads(NO2)}}$ value increases as the charge transfer of NO_2 gradually decreases. Near Fe−N_4, the catalyst has a moderate interaction with NO_2, which is conducive to both the activation of reactants and the regeneration of the active site, so its reaction activity is the highest.

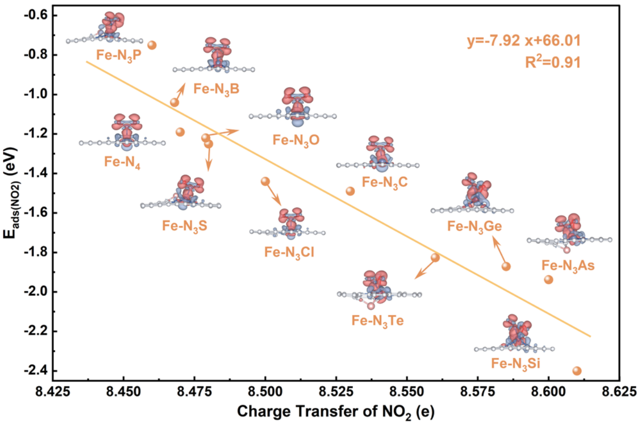

Figure 6. Correlation analysis between $E_{\mathrm{ads\ (NO2)}}$ and the charge transfer of NO_2. Contour lines in the plots are drawn at 0.002 e Å^{-3} intervals. Red and blue areas represent the electron gain and loss, respectively. Gray, light blue, blue, red, and pink atoms represent C, N, Fe, and O and doping nonmetallic atom, respectively.

4. CONCLUSIONS

The purpose of this study is to study the effect of the local coordination environment on the properties of the catalyst. In this paper, we alter the properties of the catalyst by modifying the local coordination environment of a single-atom iron catalyst, thereby achieving fine regulation of the active volcano map associated with the catalyst in the NH_3−SCR reaction. The adsorption properties of different catalysts are analyzed by the theoretical calculation. By adjusting the adsorption order of the reaction gases, the NH_3−SCR reaction paths on the Fe−N_3B catalyst are studied in detail. The results show that path 4 has the lowest rate-determining step energy barrier; therefore, it is the most likely path to occur during the reaction. After calculating the energy change of path 4 on the surface of 7 kinds of catalysts, we find that the reaction energy barrier of path 4 is linearly related to the adsorption energy of NO_2 through correlation analysis. Then, we construct a 1D volcano map model using NO_2 adsorption energy as an accurate descriptor to describe the activity of NH_3 reduction catalyzed by single-atom iron catalysts. The model is helpful in predicting the performance of different catalysts. It is found that the closer the NO_2 adsorption energy approaches −1.18 eV, the greater the theoretical catalytic activity for the NH_3 reduction becomes. We also use the model to predict the activity of 30 kinds of SACs, and the result confirms that the volcano map of single-atom iron catalysts in the NH_3−SCR reaction can be fine-tuned by regulating the local coordination environment. In addition, in order to prove the reliability of the volcano map, we also try to regulate the activity of the catalysts by doping two different nonmetal atoms on Zn−N_4 and Mn−N_4. The final results show that this regulation method brings the activity of the two catalysts closer to the peak of the volcano map and achieves a fine regulation of the activity in a small range. This study deepens the understanding of the fine-tuning catalyst activity through regulating the local coordination environment, provides a solid theoretical basis for subsequent catalyst screening and experimental preparation, and helps guide future experimental design and catalyst optimization.

■ ASSOCIATED CONTENT

Supporting Information

The Supporting Information is available free of charge at https://pubs.acs.org/doi/10.1021/acs.energyfuels.4c06055.

> Computational details; optimized structures; and calculated free-energy diagrams of reaction paths on each catalyst (PDF)

■ AUTHOR INFORMATION

Corresponding Author

Weijie Yang − *Department of Power Engineering, North China Electric Power University, Baoding 071003 Hebei, China; Hebei Key Laboratory of Low Carbon and High-Efficiency Power Generation Technology, North China Electric Power University, Baoding 071003 Hebei, China;* orcid.org/0000-0002-0232-1129; Email: yangwj@ncepu.edu.cn

Authors

Zhengyang Gao − *Department of Power Engineering, North China Electric Power University, Baoding 071003 Hebei, China; Hebei Key Laboratory of Low Carbon and High-Efficiency Power Generation Technology, North China Electric Power University, Baoding 071003 Hebei, China*

Chu Wang − *Department of Power Engineering, North China Electric Power University, Baoding 071003 Hebei, China; Hebei Key Laboratory of Low Carbon and High-Efficiency Power Generation Technology, North China Electric Power University, Baoding 071003 Hebei, China*

Mingzhe Li − *Department of Power Engineering, North China Electric Power University, Baoding 071003 Hebei, China; Hebei Key Laboratory of Low Carbon and High-Efficiency Power Generation Technology, North China Electric Power University, Baoding 071003 Hebei, China*

Ziwei Miao − *Department of Power Engineering, North China Electric Power University, Baoding 071003 Hebei, China; Hebei Key Laboratory of Low Carbon and High-Efficiency Power Generation Technology, North China Electric Power University, Baoding 071003 Hebei, China*

Yuxuan Liu − *Department of Power Engineering, North China Electric Power University, Baoding 071003 Hebei, China; Hebei Key Laboratory of Low Carbon and High-Efficiency Power Generation Technology, North China Electric Power University, Baoding 071003 Hebei, China*

Kewen Guo − *Department of Power Engineering, North China Electric Power University, Baoding 071003 Hebei, China; Hebei Key Laboratory of Low Carbon and High-Efficiency Power Generation Technology, North China Electric Power University, Baoding 071003 Hebei, China*

Yongqian Zhang − *Department of Power Engineering, North China Electric Power University, Baoding 071003 Hebei, China; Hebei Key Laboratory of Low Carbon and High-Efficiency Power Generation Technology, North China Electric Power University, Baoding 071003 Hebei, China; Haier Science and Technology Innovation Park, Haier Group, Qingdao 266000 Shandong, China*

Complete contact information is available at: https://pubs.acs.org/10.1021/acs.energyfuels.4c06055

Author Contributions

Z.G.: project administration, funding acquisition, and software. C.W.: data curation and writing—original draft. M.L., Z.M., Y.L., and K.G.: visualization. Y.Z.: theoretical calculations. W.Y.: supervision, conceptualization, funding acquisition, and writing—review and editing.

Notes

The authors declare no competing financial interest.

■ ACKNOWLEDGMENTS

This work was funded by the National Natural Science Foundation of China (Nos. 52176104 and 52006073).

■ REFERENCES

(1) Cao, Y.; Duan, Y.; Kellie, S.; Li, L.; Xu, W.; Riley, J. T.; Pan, W.-P.; Chu, P.; Mehta, A. K.; Carty, R. Impact of Coal Chlorine on Mercury Speciation and Emission from a 100-MW Utility Boiler with Cold-Side Electrostatic Precipitators and Low-NO_x Burners. *Energy Fuels* **2005**, *19* (3), 842−854.

(2) Kellie, S.; Cao, Y.; Duan, Y.; Li, L.; Chu, P.; Mehta, A.; Carty, R.; Riley, J. T.; Pan, W.-P. Factors Affecting Mercury Speciation in a 100-MW Coal-Fired Boiler with Low-NO_x Burners. *Energy Fuels* **2005**, *19* (3), 800−806.

(3) Yang, W.; Liu, X.; Chen, X.; Cao, Y.; Cui, S.; Jiao, L.; Wu, C.; Chen, C.; Fu, D.; Gates, I. D.; Gao, Z.; Jiang, H. A Sulfur-Tolerant MOF-Based Single-Atom Fe Catalyst for Efficient Oxidation of NO and Hg^0. *Adv. Mater.* **2022**, *34* (20), No. 2110123.

(4) Yang, W.; Feng, Y.; Chen, X.; Wu, C.; Wang, F.; Gao, Z.; Liu, Y.; Ding, X.; Li, H. Understanding Trends in the NO Oxidation Activity of Single-Atom Catalysts. *J. Environ. Chem. Eng.* **2022**, *10* (6), No. 108744.

(5) Jiao, A.; Zhang, H.; Liu, J.; Jiang, X. Quantum Chemical and Kinetics Calculations for the NO Reduction with Char(N): Influence of the Carbon Monoxide. *Combust. Flame* **2018**, *196*, 377−385.

(6) Liu, X.; Yang, Q. Research on the Deactivation Mechanism of a Denitration Catalyst WO_3−V_2O_5/TiO_2 at a Coal-Fired Power Plant. *RSC Adv.* **2020**, *10* (72), 44025−44033.

(7) Chen, P.; Fang, Y.; Wang, P.; Gu, M.; Luo, K.; Fan, J. The Effect of Ammonia Co-Firing on NO Heterogeneous Reduction in the High-Temperature Reduction Zone of Coal Air-Staging Combustion: Experimental and Quantum Chemistry Study. *Combust. Flame* **2022**, *237*, No. 111857.

(8) Chen, P.; Jiang, B.; Wang, H.; Gu, M.; Fang, Y.; Wang, P. Experimental and Theoretical Calculations Study on Heterogeneous Reduction of NO by Char/NH_3 in the Reduction Zone of Ammonia Co-Firing with Pulverized Coal: Influence of Mineral Fe. *Fuel* **2022**, *310*, No. 122374.

(9) Gao, Z.; Liu, X.; Li, A.; Li, X.; Ding, X.; Yang, W. Bimetallic Sites Supported on N-Doped Graphene ((Fe,Co)/N-GN) as a New Catalyst for NO Oxidation: A Theoretical Investigation. *Molecular Catalysis* **2019**, *470*, 56−66.

(10) Gao, Z.; Li, A.; Liu, X.; Ma, C.; Li, X.; Yang, W.; Ding, X. Density Functional Study of the Adsorption of NO on Ni_n (n = 1, 2, 3 and 4) Clusters Doped Functionalized Graphene Support. *Appl. Surf. Sci.* **2019**, *481*, 940−950.

(11) Zhao, S.; Peng, J.; Ge, R.; Wu, S.; Zeng, K.; Huang, H.; Yang, K.; Sun, Z. Research Progress on Selective Catalytic Reduction (SCR) Catalysts for NO_x Removal from Coal-Fired Flue Gas. *Fuel Process. Technol.* **2022**, *236*, No. 107432.

(12) Yang, Y.; Liu, J.; Wang, Z.; Yu, Y. Reaction Mechanism of Elemental Mercury Oxidation to $HgSO_4$ during SO_2/SO_3 Conversion over V_2O_5/TiO_2 Catalyst. *Proc. Combust. Inst.* **2021**, *38*, 4317−4325, DOI: 10.1016/j.proci.2020.10.007.

(13) Zhao, S.; Peng, J.; Ge, R.; Yang, K.; Wu, S.; Qian, Y.; Xu, T.; Gao, J.; Chen, Y.; Sun, Z. Poisoning and Regeneration of Commercial V_2O_5-WO_3/TiO_2 Selective Catalytic Reduction (SCR) Catalyst in Coal-Fired Power Plants. *Process Safety and Environmental Protection* **2022**, *168*, 971−992.

(14) Wang, H.; Yuan, B.; Hao, R.; Zhao, Y.; Wang, X. A Critical Review on the Method of Simultaneous Removal of Multi-Air-Pollutant in Flue Gas. *Chem. Eng. J.* **2019**, *378*, No. 122155.

(15) Zhao, S.; Peng, J.; Qian, Y.; Sun, Z. Low-Temperature $DeNO_x$ Characteristics and Mechanism of the Fe-Doped Modified CeMn Selective Catalytic Reduction Catalyst. *Fuel Process. Technol.* **2023**, *244*, No. 107704.

(16) Wang, X.; Du, X.; Zhang, L.; Chen, Y.; Yang, G.; Ran, J. Promotion of NH_4HSO_4 Decomposition in NO/NO_2 Contained Atmosphere at Low Temperature over V_2O_5-WO_3/TiO_2 Catalyst for NO Reduction. *Appl. Catal., A* **2018**, *559*, 112−121.

(17) Yang, W.; Zhou, B.; Zhang, Y.; Ren, J.; Wu, C.; Gates, I. D.; Liu, Y.; Gao, Z. A Novel Low-Temperature Fe-Fe Double-Atom Catalyst for a "Fast SCR" Reaction. *Molecular Catalysis* **2022**, *533*, No. 112769.

(18) Gao, S.; Lian, K.; Wang, X.; Liu, X.; Abdukayum, A.; Kong, Q.; Hu, G. Recent Achievements in Heterogeneous Bimetallic Atomically Dispersed Catalysts for Zn−Air Batteries: A Minireview. *Small* **2024**, *20* (51), No. 2406776.

(19) Chen, K.; Ma, D.; Zhang, Y.; Wang, F.; Yang, X.; Wang, X.; Zhang, H.; Liu, X.; Bao, R.; Chu, K. Urea Electrosynthesis from Nitrate and CO_2 on Diatomic Alloys. *Adv. Mater.* **2024**, *36* (30), No. 2402160.

(20) Liu, D.; Wan, X.; Shui, J. Tailoring Oxygen Reduction Reaction on M−N−C Catalysts via Axial Coordination Engineering. *Small* **2024**, *20* (50), No. 2406078.

(21) Liu, J.; Wan, X.; Liu, S.; Liu, X.; Zheng, L.; Yu, R.; Shui, J. Hydrogen Passivation of M−N−C (M = Fe, Co) Catalysts for Storage Stability and ORR Activity Improvements. *Adv. Mater.* **2021**, *33* (38), No. 2103600.

(22) Gao, Z.; Li, L.; Huang, H.; Xu, S.; Yan, G.; Zhao, M.; Ding, Z. Adsorption Characteristics of Acid Gases (NO, NO_2, SO_2 and SO_3) on Different Single-Atom Nickel Adsorbent: A First-Principles Study. *Appl. Surf. Sci.* **2020**, *527*, No. 146939.

(23) Yang, W.; Chen, X.; Feng, Y.; Wang, F.; Gao, Z.; Liu, Y.; Ding, X.; Li, H. Understanding Trends in the Mercury Oxidation Activity of Single-Atom Catalysts. *Environ. Sci.: Nano* **2022**, *9* (6), 2041−2050.

(24) Yang, W.; Chen, L.; Jia, Z.; Zhou, B.; Liu, Y.; Wu, C.; Gao, Z. Design of Single-Atom Catalysts for NO Oxidation Using OH Radicals. *J. Mater. Chem. A* **2023**, *11* (43), 23249−23259.

(25) Yang, W.; Ren, J.; Zhang, H.; Li, J.; Wu, C.; Gates, I. D.; Gao, Z. Single-Atom Iron as a Promising Low-Temperature Catalyst for Selective Catalytic Reduction of NO_x with NH_3: A Theoretical Prediction. *Fuel* **2021**, *302*, No. 121041.

(26) Guo, Z.; Liu, C.; Sun, C.; Xu, J.; Li, H.; Wang, T. Tuning the Coordination Environment of Single-Atom Iron Catalysts Towards Effective Nitrogen Reduction. *ChemCatChem.* **2023**, *15* (14), No. e202300669.

(27) Yang, W.; Zhou, B.; Chen, L.; Shi, R.; Li, H.; Liu, X.; Gao, Z. Coordination Engineering for Single-Atom Catalysts in Bifunctional Oxidation NO and Mercury. *Fuel* **2023**, *349*, No. 128751.

(28) Bogojeski, M.; Vogt-Maranto, L.; Tuckerman, M. E.; Müller, K.-R.; Burke, K. Quantum Chemical Accuracy from Density Functional Approximations via Machine Learning. *Nat. Commun.* **2020**, *11* (1), No. 5223.

(29) Kresse, G.; Furthmüller, J. Efficiency of Ab-Initio Total Energy Calculations for Metals and Semiconductors Using a Plane-Wave Basis Set. *Comput. Mater. Sci.* **1996**, *6* (1), 15−50.

(30) Kresse, G.; Joubert, D. From Ultrasoft Pseudopotentials to the Projector Augmented-Wave Method. *Phys. Rev. B* **1999**, *59* (3), 1758−1775.

(31) Jing, N.; Xue, Q.; Ling, C.; Shan, M.; Zhang, T.; Zhou, X.; Jiao, Z. Effect of Defects on Young's Modulus of Graphene Sheets: A Molecular Dynamics Simulation. *RSC Adv.* **2012**, *2* (24), 9124.

(32) Perdew, J. P.; Burke, K.; Ernzerhof, M. Generalized Gradient Approximation Made Simple. *Phys. Rev. Lett.* **1996**, *77* (18), 3865−3868.

(33) Krasheninnikov, A. V.; Lehtinen, P. O.; Foster, A. S.; Pyykkö, P.; Nieminen, R. M. Embedding Transition-Metal Atoms in Graphene: Structure, Bonding, and Magnetism. *Phys. Rev. Lett.* **2009**, *102* (12), No. 126807.

(34) Lin, C.; Liu, X.; Qu, J.; Feng, X.; Seh, Z. W.; Wang, T.; Zhang, Q. Strain-Controlled Single Cr-Embedded Nitrogen-Doped Graphene Achieves Efficient Nitrogen Reduction. *Mater. Adv.* **2021**, *2* (17), 5704−5711.

(35) Vojvodic, A.; Nørskov, J. K.; Abild-Pedersen, F. Electronic Structure Effects in Transition Metal Surface Chemistry. *Top. Catal.* **2014**, *57* (1−4), 25−32.

(36) Bhattacharjee, S.; Waghmare, U. V.; Lee, S.-C. An Improved D-Band Model of the Catalytic Activity of Magnetic Transition Metal Surfaces. *Sci. Rep.* **2016**, *6* (1), No. 35916.

(37) Chan, K. T.; Neaton, J. B.; Cohen, M. L. First-Principles Study of Metal Adatom Adsorption on Graphene. *Phys. Rev. B* **2008**, *77* (23), No. 235430.

(38) Yan, G.; Gao, Z.; Zhao, M.; Ma, K.; Ding, Z.; Yang, W.; Ding, X. Mechanism Study on CO_2 Reforming of Methane over Platinum Cluster Doped Graphene: A DFT Calculation. *Molecular Catalysis* **2020**, *497*, No. 111205.

(39) Liu, H.; Yang, L.; Qiao, K.; Zeng, X.; Huang, Y.; Zheng, L.; Cao, D. A New Concept Analogous to Homogeneous Catalysis to Construct In-Situ Regenerative Electrodes for Long-Term Oxygen Evolution Reaction. *Nano Energy* **2020**, *76*, No. 105115.

(40) Henkelman, G.; Uberuaga, B. P.; Jónsson, H. A Climbing Image Nudged Elastic Band Method for Finding Saddle Points and Minimum Energy Paths. *J. Chem. Phys.* **2000**, *113* (22), 9901−9904.

(41) Dong, J.; Gao, Z.; Yang, W.; Li, A.; Ding, X. Adsorption Characteristics of Co-Anchored Different Graphene Substrates toward O_2 and NO Molecules. *Appl. Surf. Sci.* **2019**, *480*, 779−791.

(42) Heyden, A.; Bell, A. T.; Keil, F. J. Efficient Methods for Finding Transition States in Chemical Reactions: Comparison of Improved Dimer Method and Partitioned Rational Function Optimization Method. *J. Chem. Phys.* **2005**, *123* (22), No. 224101.

(43) Deringer, V. L.; Tchougréeff, A. L.; Dronskowski, R. Crystal Orbital Hamilton Population (COHP) Analysis As Projected from Plane-Wave Basis Sets. *J. Phys. Chem. A* **2011**, *115* (21), 5461−5466.

(44) Siegel, D. J.; Hector, L. G.; Adams, J. B. Adhesion, Atomic Structure, and Bonding at the Al (111)/α−Al_2O_3(0001) Interface: A First Principles Study. *Phys. Rev. B* **2002**, *65* (8), No. 085415.

(45) Tozini, D.; Forti, M.; Gargano, P.; Alonso, P. R.; Rubiolo, G. H. Charge Difference Calculation in Fe/Fe_3O_4 Interfaces from DFT Results. *Procedia Materials Science* **2015**, *9*, 612−618.

(46) Bligaard, T.; Nørskov, J. K.; Dahl, S.; Matthiesen, J.; Christensen, C. H.; Sehested, J. The Brønsted−Evans−Polanyi Relation and the Volcano Curve in Heterogeneous Catalysis. *J. Catal.* **2004**, *224* (1), 206−217.

(47) Yang, W.; Ren, J. Single-Atom Iron as a Promising Low-Temperature Catalyst for Selective Catalytic Reduction of NO_x with NH_3: A Theoretical Prediction. 2021.

(48) Montemore, M. M.; Medlin, J. W. Predicting and Comparing C−M and O−M Bond Strengths for Adsorption on Transition Metal Surfaces. *J. Phys. Chem. C* **2014**, *118* (5), 2666−2672.

(49) Montemore, M. M.; Medlin, J. W. Scaling Relations between Adsorption Energies for Computational Screening and Design of Catalysts. *Catal. Sci. Technol.* **2014**, *4* (11), 3748−3761.

(50) Nørskov, J. K.; Bligaard, T.; Logadottir, A.; Bahn, S.; Hansen, L. B.; Bollinger, M.; Bengaard, H.; Hammer, B.; Sljivancanin, Z.; Mavrikakis, M.; Xu, Y.; Dahl, S.; Jacobsen, C. J. H. Universality in Heterogeneous Catalysis. *J. Catal.* **2002**, *209* (2), 275−278.

(51) Medford, A. J.; Vojvodic, A.; Hummelshøj, J. S.; Voss, J.; Abild-Pedersen, F.; Studt, F.; Bligaard, T.; Nilsson, A.; Nørskov, J. K. From the Sabatier Principle to a Predictive Theory of Transition-Metal Heterogeneous Catalysis. *J. Catal.* **2015**, *328*, 36−42.